Electrothermally actuated tip-tilt-piston micromirror with integrated varifocal capability

Jessica Morrison,[1,*] Matthias Imboden,[2] Thomas D.C. Little,[2] and D. J. Bishop[1,2,3]

[1]*Department of Physics, Boston University, Boston, Massachusetts, USA*
[2]*Department of Electrical and Computer Engineering, Boston University, Boston, Massachusetts, USA*
[3]*Division of Materials Science and Engineering, Boston University, Brookline, Massachusetts, USA*
[*]*Jessica.Morrison04@gmail.com*

Abstract: MEMS micromirrors have proven to be very important optical devices with applications ranging from steerable mirrors for switches and cross-connects to spatial light modulators for correcting optical distortions. Usually beam steering and focusing are done with different MEMS devices and tilt angles in excess of 10 degrees are seldom obtained. Here we describe a single MEMS device that combines tip/tilt, piston mode and varifocal capability into a single, low cost device with very large tilt angles. Our device consists of a 400 micron diameter mirror driven with thermal bimorphs. We have demonstrated deflection angles of ± 40 degrees along both axes, a tunable focal length which varies between −0.48 mm to + 20.5 mm and a piston mode range of 300 microns - four separately controllable degrees of freedom in a single device. Potential applications range from smart lighting to optical switches and devices for telecom systems.

OCIS codes: (060.2605) Free-space optical communication; (060.4510) Optical communications; (110.1080) Active or adaptive optics; (130.3990) Micro-optical devices; (230.4685) Optical microelectromechanical devices.

References and links

1. D. L. Dickensheets, "Requirements of MEMS membrane mirrors for focus adjustment and aberration correction in endoscopic confocal and optical coherence tomography imaging instruments," J. Micro/Nanolithography. MEMS. MOEMS **7**(2), 021008 (2008).
2. W. Noell, P. A. Clerc, L. Dellmann, B. Guldimann, H. P. Herzig, O. Manzardo, C. R. Marxer, K. J. Weible, R. Dändliker, and N. De Rooij, "Applications of SOI-based optical MEMS," IEEE J. Sel. Top. Quantum Electron. **8**(1), 148–154 (2002).
3. V. A. Aksyuk, F. Pardo, D. Carr, D. Greywall, H. B. Chan, M. E. Simon, A. Gasparyan, H. Shea, V. Lifton, C. Bolle, S. Arney, R. Frahm, M. Paczkowski, M. Haueis, R. Ryf, D. T. Neilson, S. Member, J. Kim, C. R. Giles, and D. Bishop, "Beam-Steering Micromirrors for Large Optical Cross-Connects," J. Lightwave Technol. **21**(3), 634–642 (2003).
4. B. Qi, A. Phillip Himmer, L. Maggie Gordon, X. D. Victor Yang, L. David Dickensheets, and I. Alex Vitkin, "Dynamic focus control in high-speed optical coherence tomography based on a microelectromechanical mirror," Opt. Commun. **232**(1-6), 123–128 (2004).
5. T. Sasaki and K. Hane, "Initial deflection of silicon-on-insulator thin membrane micro-mirror and fabrication of varifocal mirror," Sens. Actuators A Phys. **172**(2), 516–522 (2011).
6. R. Hokari and K. Hane, "Micro-mirror laser scanner combined with a varifocal mirror," Microsyst. Technol. **18**(4), 475–480 (2012).
7. M. J. Booth, "Adaptive optical microscopy: the ongoing quest for a perfect image," Light Sci. Appl. **3**(4), e165 (2014).
8. M. Strathman, Y. Liu, X. Li, and L. Y. Lin, "Dynamic focus-tracking MEMS scanning micromirror with low actuation voltages for endoscopic imaging," Opt. Express **21**(20), 23934–23941 (2013).
9. T. Sandner, "Translatory MEMS actuators for optical path length modulation in miniaturized Fourier-transform infrared spectrometers," J. Micro/Nanolithography. MEMS MOEMS **7**(2), 021006 (2008).
10. S. Schweizer, S. Calmes, M. Laudon, and P. Renaud, "Thermally actuated optical microscanner with large angle and low consumption," Sens. Actuators A Phys. **76**(1-3), 470–477 (1999).
11. J. Singh, C. C. Hoe, T. H. S. Jason, C. Nanguang, C. S. Premachandran, C. J. R. Sheppard, and M. Olivo, "Optical coherent tomography (OCT) bio-imaging using 3D scanning micromirror," Proc. SPIE **6432**, C4320 (2007).

#235441 - $15.00 USD Received 5 Mar 2015; revised 26 Mar 2015; accepted 26 Mar 2015; published 3 Apr 2015

12. A. Jain, H. Qu, S. Todd, and H. Xie, "A thermal bimorph micromirror with large bi-directional and vertical actuation," Sens. Actuators A Phys. **122**(1), 9–15 (2005).
13. K. Jia, S. Pal, and H. Xie, "An electrothermal tip-tilt-piston micromirror based on folded dual s-shaped bimorphs," J. Microelectromech. Syst. **18**(5), 1004–1015 (2009).
14. S. R. Davis, G. Farca, S. D. Rommel, A. W. Martin, and M. H. Anderson, "Analog, non-mechanical beam-steerer with 80 degree field of regard," Proc. SPIE **6971**, 69710G (2008).
15. W. Liu and J. J. Talghader, "Current-controlled curvature of coated micromirrors," Opt. Lett. **28**(11), 932–934 (2003).
16. J. Y. Tsao, M. H. Crawford, M. E. Coltrin, A. J. Fischer, D. D. Koleske, G. S. Subramania, G. T. Wang, J. J. Wierer, and R. F. Karlicek, "Toward Smart and Ultra-efficient Solid-State Lighting," Adv. Opt. Mater. **2**(9)809–836 (2014).
17. P. Brandl, S. Member, S. Schidl, A. Polzer, W. Gaberl, H. Zimmermann, and S. Member, "Focus and MEMS-Based Beam Steering," IEEE Photon. Technol. Lett. **25**(15), 1428–1431 (2013).
18. D. Koester, A. Cowen, and R. Mahadevan, "PolyMUMPs design handbook," http://www.memscap.com/products/mumps/polymumps/reference-material.
19. W.-H. Chu, M. Mehregany, and R. L. Mullen, "Analysis of tip deflection and force of a bimetallic cantilever microactuator," J. Micromech. Microeng. **3**(1), 4–7 (1993).
20. S. T. Todd, S. Member, H. Xie, and S. Member, "An Electrothermomechanical Lumped Element Model of an Electrothermal Bimorph Actuator," J. Microelectromech. Syst. **17**(1), 213–225 (2008).
21. J. Zou, M. Balberg, C. Byrne, C. Liu, and D. J. Brady, "Optical properties of surface micromachined mirrors with etch holes," J. Microelectromech. Syst. **8**(4), 506–513 (1999).
22. L. Wu and H. Xie, "A large vertical displacement electrothermal bimorph microactuator with very small lateral shift," Sens. Actuators A Phys. **145-146**, 371–379 (2008).
23. J. Sun, S. Guo, L. Wu, L. Liu, S.-W. Choe, B. S. Sorg, and H. Xie, "3D in vivo optical coherence tomography based on a low-voltage, large-scan-range 2D MEMS mirror," Opt. Express **18**(12), 12065–12075 (2010).
24. K. Gall, M. L. Dunn, Y. Zhang, and B. Corff, "Thermal cycling response of layered gold/polysilicon MEMS structures," Mech. Mater. **36**(1-2), 45–55 (2004).
25. E. Merced, S. Member, X. Tan, S. Member, N. Sepúlveda, and S. Member, "Closed-Loop Tracking of Large Displacements in Electro-Thermally Actuated VO2-Based MEMS," J. Microelectromech. Syst. **23**, 1073–1083 (2014).

1. Introduction

Microelectromechanical systems (MEMS) are used for beam deflection and shaping in a wide range of applications. They are utilized in range finders, optical coherence tomography (OCT) [1], as well as in many other processes such as confocal microscopy, Fourier transform spectroscopy [2] and in optical cross connects [3] for communication hubs. Varifocal micromirrors have been shown to improve lateral resolution of an image without reducing the depth of focus [4,5]. Both scanning and varifocal micromirrors have been combined in a single system to add flexibility to optical sensing systems [6]. Commercially available deformable mirrors that employ MEMS as their backbone are now a common method of reducing astigmatisms and other aberrations, increasing the resolution [7]. In more recent research, micromirrors capable of dynamic focus as well as 2D scanning have been fully integrated [8]. Such devices rely on electrostatic actuation for both focus and beam deflection. This method results in negligible power consumption for mechanical deflections on the order of ± 5° and a dynamic focus range from infinity to −25 mm. In contrast to electrostatic devices, mirrors which use electrothermal actuation allow for large deflection range in 1D MEMS [9], and higher dimensional microsystems [10–13]. Refractive systems using liquid crystals can also obtain very large steering angles but also require ~100 V to operate [14]. Electrothermal bimorph membranes have been used for current controlled tunable focus with a 2-3 mm focal range [15].

This paper presents a micromirror design using electrothermal actuation for beam steering along two axes, piston mode deflections and dynamic focusing — four separately controllable degrees of freedom in a single device. The focal length can be dynamically changed from −0.48 mm to + 20.5 mm with 27 mW of power. Additionally, it has an optical deflection range of ± 40° along both lateral axes. Furthermore, by actuating all of the bimorph legs simultaneously, the mirror can be actuated in piston mode providing a fourth degree of freedom with a 300 µm vertical range.

#235441 - $15.00 USD Received 5 Mar 2015; revised 26 Mar 2015; accepted 26 Mar 2015; published 3 Apr 2015

One application for this device is in smart lighting, a non-imaging system in which MEMS can be integrated with solid state lighting to enable complete control over the flux and the chromaticity of a lighting fixture [16]. A subset of the smart lighting applications includes MEMS in optical communication systems. A combination of macroscopic adaptive optics and a scanning micromirror have been used to increase the signal to noise ratio in an optical wireless communications (OWC) setup [17]. Our mirror eliminates the need for additional optics to provide fully integrated directional light. Beam steering can provide dynamic OWC for mobile systems while the tunable focus can be used in location algorithms to pinpoint the location of a receiver and focus on it. Our device has a mechanical response time of approximately 5 ms, faster than the response time of the human eye. Micromirrors provide a cheap and effective method of introducing chip level control of illumination in both space and time [16]. Our device, by combing all the relevant degrees of freedom into a single, low cost chip, can add this functionality to solid state lighting systems in a practical way.

2. Device design and actuation

2.1 Design

The micromirror device shown in Fig. 1(a) is fabricated using a Multi-User MEMS Process (MUMPs) known as PolyMUMPs by MEMSCAP [18]. The fabrication includes three highly doped polysilicon layers, two sacrificial oxide layers, and a gold layer patterned using optical lithography. Residual compressive stresses in the polysilicon layer combined with residual tensile stresses in the gold layer due to the fabrication process provide a stress gradient along the boundary of the gold and polysilicon layers. Upon release, a bending strain due to the stress in the bimorph structures provides an initial curvature as shown in Fig. 1(b). Bimorph actuators rely on a difference in coefficients of thermal expansion (CTE) of the two layers. The CTE of the gold layer is greater than that of the polysilicon resulting in a temperature dependent curvature [19], κ, given as:

$$\kappa \equiv \frac{1}{r} = \frac{1}{r_0} + \frac{6t(\alpha_{Au} - \alpha_{Si})\Delta T}{4t_{Au}^2 + 4t_{Si}^2 + 6t_{Au}t_{Si} + \left(\frac{E_{Au}t_{Au}^3}{E_{Si}t_{Si}}\right) + \left(\frac{E_{Si}t_{Si}^3}{E_{Au}t_{Au}}\right)} \tag{1}$$

where r is the temperature dependent radius of curvature, r_0 is the initial radius of curvature at room temperature, t is the sum of the individual layer thicknesses, t_{Au}, and t_{Si}, α_{Au} and α_{Si} are the temperature coefficients of expansion for each layer, E_{Au} and E_{Si} are the Young's Moduli of each layer, and ΔT is the temperature change.

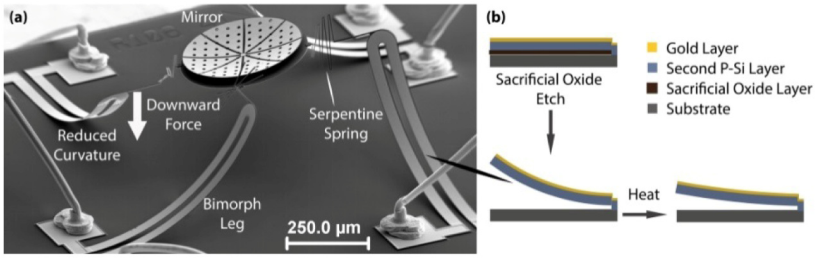

Fig. 1. (a) SEM image of micromirror device. (b) Illustration of bimorph layers before and after oxide etch and reduced curvature due to heating.

Four bimorphs are positioned tangential to the mirror acting as the "legs" to raise the mirror above the substrate upon release. Side-angle views of the bimorph legs are shown in Fig. 1(b). The curvature, and therefore the tip height, of each bimorph leg can be finely tuned using Joule heating to deflect the mirror toward the substrate as is illustrated in Fig. 1(a). To

#235441 - $15.00 USD Received 5 Mar 2015; revised 26 Mar 2015; accepted 26 Mar 2015; published 3 Apr 2015

first order, the temperature change due to Joule heating in a resistor is linearly proportional to the electrical power, $\Delta T \propto I^2 \cdot R(T)$. Gold has a positive resistance temperature coefficient and as a result, when current biasing the system the power and temperature form a positive feedback loop prior to thermal equilibrium. When voltage biasing the bimorph, there is an initial power peak increasing the rate at which the thermal equilibrium is established. Voltage biasing avoids the runaway power increase possible when current biasing and is typically the drive method of choice for systems with positive thermal resistance coefficients [20]. However, as the resistance of the bimorph legs is typically the same order of magnitude of the resistance of the connected leads, a current bias provides better stability and control when a four point probe is unavailable.

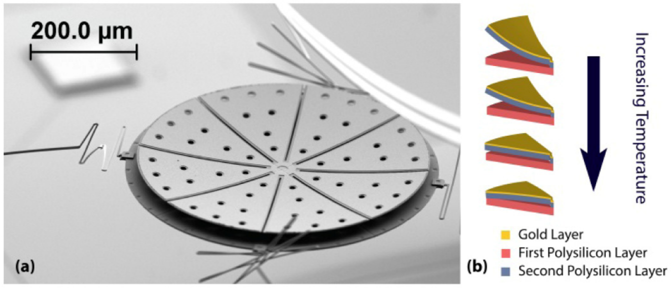

Fig. 2. (a) SEM image of the mirror depicting the eight bimorph wedges and (b) an illustration of the wedge shape as Joule heating in the serpentine springs heats the platform and mirror.

Each of the four bimorph legs is connected, at the tip, to a polysilicon serpentine spring of 3.75 μm^2 cross sectional area, 160 μm arm length and composed of 5 turns. These springs have a dual function: 1) they enable the bending, extension and twisting required to allow the mirror to be tilted to large angles and 2) as describe in detail below, the springs serve as local heaters for the central plate. While the serpentine springs are flexible enough to allow for large angles, frequency response measurements have shown a vertical (piston-mode) resonant frequency of ~700 Hz. As an order of magnitude approximation, the displacement of mirror under only gravitational forces can be approximated by $\delta \approx g/\omega_0^2 \approx 500\text{nm}$, where $g = 10\ \text{m/s}^2$. This demonstrates that while the springs provide enough flexibility for angular deflection, the position of the mirror does not significantly deviate in response to low frequency noise. The springs are connected to a circular polysilicon platform, 400 μm in diameter. Eight polysilicon and gold bimorph wedges extend from the center of the platform which acts as the thermal contact for the mirror wedges. The wedge shape is depicted in Fig. 2(b) from an unactuated state (top) to a heated state (bottom). By segmenting the mirror into eight individual wedges, the bimorphs can deflect to a much greater degree than would be possible with a solid membrane. The long silicon springs thermally isolate the mirror from the bimorph legs.

2.2 Actuation

The device has three electrothermal actuation modes which can be controlled independently. The scanning modes are achieved by applying a current $I_{\pm\theta}$ and/or $I_{\pm\varphi}$, shown in Fig. 3. Much of the resulting current is directed along the gold layer of the bimorph as a result of the metal having much greater electrical conductivity than polysilicon. The room temperature resistance of the serpentine springs is $R_{sp} \approx 10\ \text{k}\Omega$, 1500 times larger than the bimorph leg resistance, $R_b \approx 4.5\ \Omega$. The impedance mismatch of the serpentine springs and bimorph legs allows for decoupling of the focal electrothermal actuation and deflection electrothermal actuation. Additionally, the 3.75 μm^2 cross sectional area and significant length of the springs creates a thermal barrier through which heat due to actuation of the bimorph legs is impeded. Although the power required to heat the serpentine springs is approximately the same as is

#235441 - $15.00 USD Received 5 Mar 2015; revised 26 Mar 2015; accepted 26 Mar 2015; published 3 Apr 2015

required to heat the bimorphs, the current required to heat the serpentine springs is two orders of magnitude less than is required to heat the bimorphs. As a result, the power dissipated in the bimorph legs due to the current provided to heat the mirror, I_f, is negligible compared to the power required to heat the legs. To determine the leakage power through the serpentine springs due to the actuation of a single bimorph, the leakage current through each of the four springs can be calculated using the potential at the tip of the actuated bimorph. In this case, the power ratio dissipated in the springs with respect to the bimorph scales as $9R_b/64R_{sp}$ for the nearest spring and $R_b/64R_{sp}$ for the other three springs. The piston mode is available by actuating all four legs at the same power.

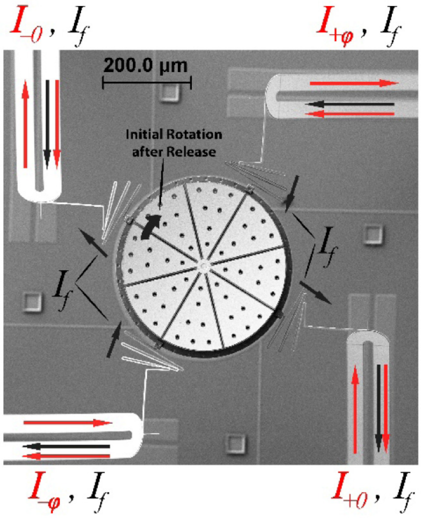

Fig. 3. SEM image with an actuation overlay. Eight electrical leads are used to control both deflection and variable focus. Leakage current through the springs due to $I_{\pm\theta/\varphi}$ results in negligible power consumption and is not shown here.

Heating the mirror wedges changes their curvature. This deflection dictates the dynamic focal length as the radius of curvature is twice the focal length, $f = r/2$. By introducing a current, I_f between any of the two legs, as shown in Fig. 3, the serpentine springs can be heated. The highly doped silicon also has a positive resistance temperature coefficient resulting in an increase in resistance to from $R_{sp}(T_{room}) \approx 10$ kΩ to $R_{sp}(T_{hot}) \approx 14$ kΩ. The thermal energy in the springs flows to the platform and the mirror bimorph wedges, flattening them from their initial curved position. The resistance of the bimorph legs increase from $R_b(T_{room}) \approx 4.5$ Ω to $R_b(T_{hot}) \approx 6.0$ Ω when heated. Thus, at any temperature, the power dissipated in the springs due to leakage current from the bimorphs is two orders of magnitude less than is required to flatten the mirror.

3. Measurements and discussion

3.1 Variable focus

The focal range was characterized with an optical surface profiler. Figure 4 depicts mirror curvature measurements as the mirror is actuated. Figure 4(a) is a measurement of the average radial height of the mirror relative to the center. For no actuation, ($P_f = 0$ mW) a focal length of −0.48 mm is measured. This can be tuned to 20.5 mm by providing 1.5 mA of current ($P_f = 27$ mW) to the mirror such that each spring dissipates 6.75 mW.

#235441 - $15.00 USD Received 5 Mar 2015; revised 26 Mar 2015; accepted 26 Mar 2015; published 3 Apr 2015

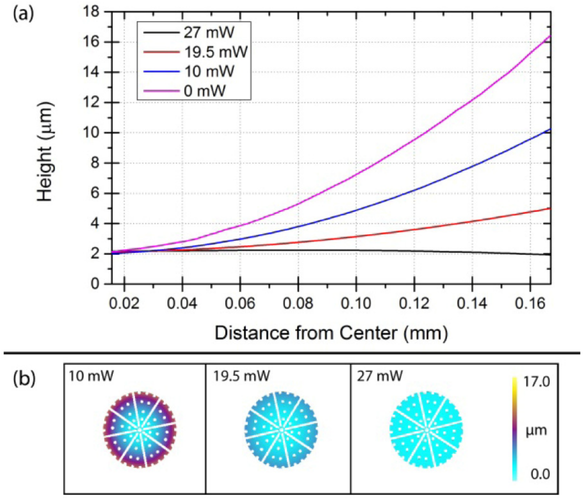

Fig. 4. Optical profiler measurements of (a) the average radial profile from the center of the mirror, (b) a surface plot for three actuation powers.

The curvature, $\kappa = 1/(2f)$, shown in Fig. 5 was measured by fitting a sphere to the gold layer profile. The central thermal contact provides a unique advantage as any temperature distribution originating from the springs is inconsequential to the thermal distribution on the wedges, as they are essentially heated from a point source at the center. As a result, any asymmetry in power dissipated between the springs does not degrade the optical properties of the mirror. The curvature when the mirror is unactuated is dependent on an initial thermal treatment and can be tuned to obtain the desired minimum focal length by altering annealing times and temperatures. The minimum focal length is also dependent on the initial maximum actuation power, P_f, which determines the level of self-annealing. All subsequent actuations are kept below the first maximum power to ensure reproducibility.

The upper limit on curvature is determined by the 2 µm proximity of circular platform beneath the wedges. The most significant aberrations, measured using Zernike polynomials, were spherical aberration, astigmatism and coma and are shown in Fig. 5(b). The spherical aberrations were consistently within ±300 nm, where the astigmatism and coma aberrations fall in the 0-200 nm range, until the last measurement where the curvature error was on the same order as the aberrations (P_f>26 mW) and the wedges were in contact with the platform. This effect can be eliminated by replacing the platform with a rim and radial attachments allowing the wedges to deflect beyond the rim.

The reflectivity of the mirror is largely governed by the surface area and scattering due to the release holes. The release holes reduce the surface area by approximately 5% and the surface area of the segment dividers reduces the effective mirror size by approximately 9%. In all, the reflectivity of the mirror is 14% less than a solid membrane before accounting for scattering and diffraction losses. The surface areal losses can be reduced by complete elimination of the release holes which would subsequently increase the etch time. This would also reduce scattering and diffraction losses. A more detailed study is required to understand fully the overall optical losses as they are largely dependent on the angle of incidence and the wavelength of the incident light [21].

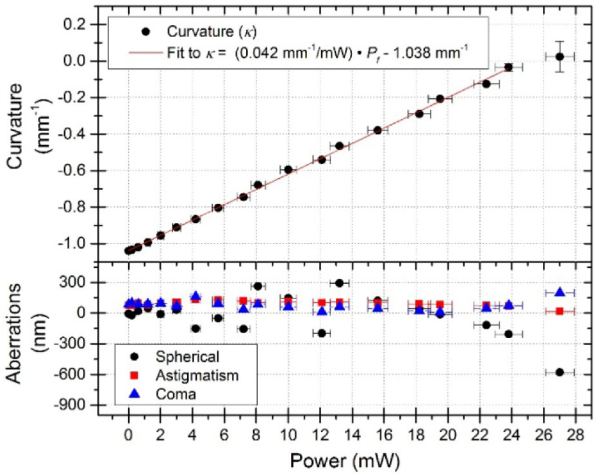

Fig. 5. Curvature (top) and Zernike aberrations (bottom) versus power based on a spherical fit to the optical profile of the gold layer. The curvature is fit to $\kappa = (0.042\ \text{mm}^{-1}/\text{mW}) \cdot P_f$ mW $-1.038\ \text{mm}^{-1}$ with the exception of the last point where the wedges come into contact with the platform.

3.2 Beam steering

Electrothermal actuation has proven to be a promising design for large angle mechanical deflections in MEMS. Vertical (piston mode) displacements of over 600 µm [22] have been achieved with minimal lateral deflection. Additionally, optical beam deflections of over ± 30° have been obtained using electrothermal actuators [23].

The optical deflection range of the MEMS present here is shown in Fig. 6. The out of plane projection of the bimorphs following the oxide etch forces a rotation of the mirror about the vertical axis, illustrated in Fig. 3. Thus, if a single bimorph is actuated the mirror pivots such that the axis of rotation is not constant and the symmetry of the four bimorphs is lost. To reduce rotation of the mirror and platform, the baseline mirror height is decreased by actuating two of the four bimorphs at an offset power, P_0. The other two bimorphs are actuated using a differential power based on the initial current-voltage measurements. The power is produced with a current bias such that $P_{\theta,\varphi} = P_1 \pm P_{Tilt}$, where P_1 = 15 mW is held constant at half the maximum power and P_{Tilt} is varied between 0 mW and 15 mW. The error in P_{Tilt} is dominated by the temperature dependence of the resistance and results in an asymmetric power differential between legs. Two scenarios are shown in Fig. 6, the first with P_0 = 15 mW yielding a total constant power of 60 mW and the second with P_0 = 30 mW yielding a constant total power of 90 mW. When P_0 = 15 mW, the angular deflection is linearly proportional to the differential applied power, P_{Tilt}. Furthermore, the beam deflection along the θ and φ axes are kept independent of one other, providing a straightforward trigonometric relationship between the Cartesian coordinates of the reflected spot on a screen and power provided to the bimorph legs. Increasing the offset power to P_0 = 30 mW increases the maximum optical deflection. However, the angular deflection at low P_{tilt} is no longer linearly proportional to P_{Tilt} because the mirror pivot point is not held constant. The asymmetry causes the axis of rotation to shift for each actuation power such that the beam deflection does not follow a straight line, convoluting the relationship between deflection angle magnitude and beam direction.

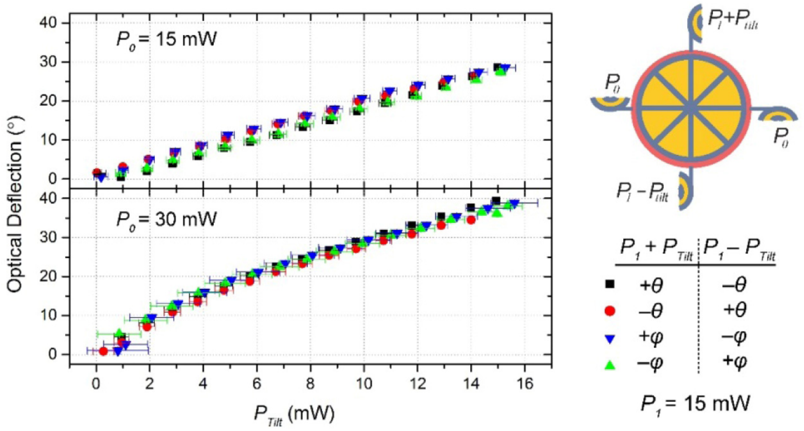

Fig. 6. Beam deflection angle is plotted against actuation power when P_0 = 15 mW and when P_0 = 30 mW (left). At the right is a diagram illustrating the powers of the bimorph legs during actuation. The labels for the power provided to each leg are given as subscripts ± θ and ± φ as shown in Fig. 3.

Actuation of all four bimorph legs results in a piston mode vertical deflection. The vertical displacement is plotted in Fig. 7 versus the total power provided to the four bimorph legs. As the mirror is pulled toward the substrate, heat from the bimorph legs flows to the mirror and the minimum focal length is increased slightly to −0.87 mm. The reduction of focal range due to actuating all four bimorph legs is a worst case scenario for the mirror as the total heat needed for maximum tilt is lower than the heat applied for full vertical actuation. However, it must be noted that the piston and tip-tilt actuation modes are coupled. Actuating a mirror vertically reduces the tip/tilt range, as now $P_{\theta,\varphi}$, P_0 and P_1 are constrained.

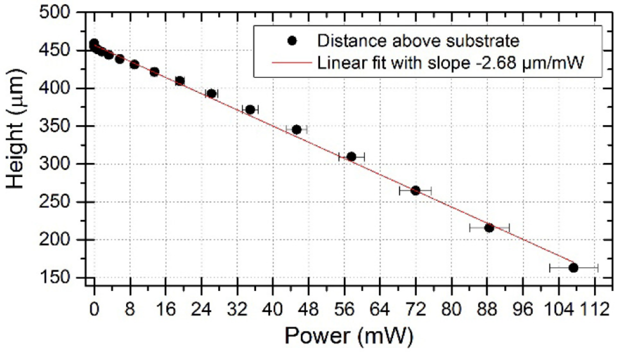

Fig. 7. Shown is the height above the substrate of the center of the micromirror as all four bimorph legs are actuated at the same power together. The red trace is a linear fit with a slope of −2.68 μm/mW.

Thermal cycling effects in the bimorphs limit curvature reproducibility and contribute to a deflection spread of approximately 3° during the first actuation. As previously mentioned, the first actuation of the mirror produces a nonlinear curvature vs. power relationship while the bimorphs self-anneal. A study on bimorph thermal cycling has been performed by Gall et al. [24]. The thermal cycling study, however, does not include temperature gradients due to electrothermal actuation. A more detailed study of the mirror cycling is required to ensure long term stability and deflection accuracy and is the focus of future work. The reproducibility of the system can be greatly improved upon by moving from the open-loop feedback control currently used to closed-loop feedback system [25] with either a power or a position sensitive PID loop.

3.3 Dynamic control

The time dependent thermal response characterization was performed by applying a current or voltage pulse to the bimorph legs and the serpentine springs. For the legs, the power resulting from the current pulse corresponded to an optical deflection angle from approximately 10° to 28°. Likewise a current pulse resulting in a radius of curvature change from $-1\ \text{mm}^{-1}$ to $+0.05\ \text{mm}^{-1}$ was used to measure the thermal response time of the mirror. The thermal time constant, τ_{th}, is determined by fitting the measured resistance to the exponential function, $R(t) = R_0 + R_1 \cdot \exp(-(t-t_0)/\tau_{th})$, where $R(t)$ is the time dependent resistance, R_0 is the resistance at low power, R_1 is the change is resistance, t *is* the time and t_0 is the time when the step in current occurred. The bimorph leg time constants were measured to be 2.0 ms to heat the bimorph legs, while the cooling time constant was 2.5 ms (data shown in Fig. 8(a)). The serpentine springs and central plate/mirror have a thermal time constant of 14.9 ms while heating and 11.7 ms while cooling as determined from the data shown in Fig. 8(b).

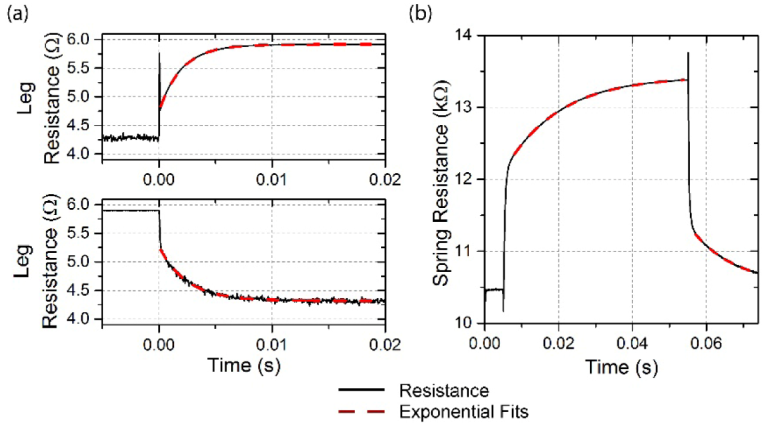

Fig. 8. Resistance measurements and exponential decay fits to $R(t) = R_0 + R_1 \cdot \exp(-(t-t_0)/\tau_{th})$ for a current pulse through (a) a bimorph leg and (b) the serpentine springs. The thermal time constants for the bimorph leg and mirror respectively were 2.0 ms and 14.9 ms for a step up in current and 2.5 ms and 11.7 ms for a step down in current.

The difference in heating and cooling thermal time constants can be attributed to changing material properties with changing temperature [20]. Furthermore, when a current flows through the legs power is generated along the entire structure, rapidly heating the bimorph. When cooling all thermal power must flow to the base, resulting in a faster heating time constant than cooling time constant. This is the reverse for the mirror where heating is locally restricted to the serpentine springs. The thermal energy must then flow onto the mirror structure. The considerable surface area allows for thermal cooling directly to the surrounding air. Consequently, the mirror cools faster than it heats. A more detailed measurement of the thermal distribution is required to make assumptions regarding the temperature of the mirror wedges and springs. The slight reduction in curvature when actuating the legs indicates that the spring provides a considerable thermal barrier between the legs and the platform.

The mechanical response times of the mirror deflection were measured by detecting reflected light from the mirror with a position sensitive detector (PSD). All of the mechanical response measurements were driven with a voltage bias. The initial peak in power with a voltage bias due to the positive temperature coefficient of resistance results in shorter response times compared to a current biased drive. To improve the accuracy of the PSD measurements, the mirror was flattened to minimize the spot size of the reflected light by

Received 5 Mar 2015; revised 26 Mar 2015; accepted 26 Mar 2015; published 3 Apr 2015

keeping P_f at a constant 26 mW. Figure 9 demonstrates the PSD measured response as a function of time when a voltage ramp is used to actuate a single leg. Three voltage drive schemes were implemented to reduce ringing and overshoot. The voltage steps all correspond to a power modulation of 0.02-27 mW (0-25° optical deflection), corresponding to an linear voltage ramp either increased from 10 mV to 400 mV or decreased from 400 mV to 10 mV over 5 ms, 1 ms or less than 100 μs (hereon referred to as a "step"). The mechanical rise time of the mirror, defined by the time required to deflect from 10% to 90% of the 25° deflection, is given in Table 1 for each drive scheme. Also included in Table 1 are the mechanical settling times defined as the time required for the system to equilibrate to within 1% of the final angle.

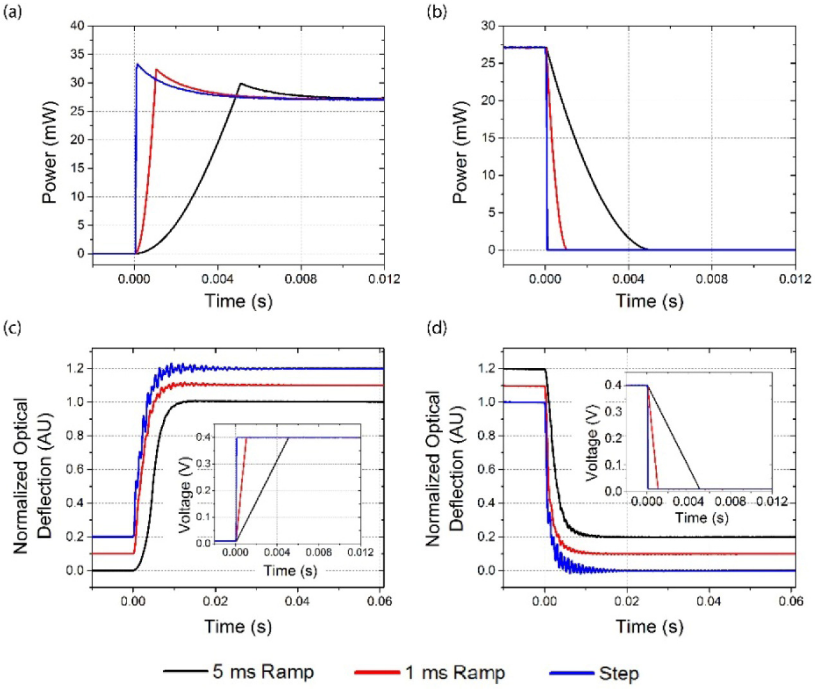

Fig. 9. (a) and (b) show the power dissipated in the bimorph leg based on the voltage ramp time, (c) and (d) are the normalized deflection angles due to the voltage ramps measured using a PSD for each of the ramp times (inset graphs provide the actual voltage over time). The normalizations (c) and (d) are each offset to reduce overlap.

Table 1. Time Response of Micromirror Deflection

Voltage Ramp Time	Rise Time	Rise Angle Overshoot	Rise Settling Time	Fall Time	Fall Angle Overshoot	Fall Settling Time
5 ms	5.2 ms	< 1%	12 ms	4.1 ms	< 1%	7 ms
1 ms	4.4 ms	1.7%	18 ms	3.1 ms	< 1%	10 ms
Step (<0.1 ms)	4.8 ms	3.0%	21 ms	2.2 ms	1.9%	14 ms

A drastic reduction in ringing is clear for the responses of both rising and falling actuation voltages in Figs. 9(c) and 9(d) when the voltage is ramped over 5 ms compared to a step in bias. However, the rise times for the step voltage and 5 ms ramp differ by less than 0.5 ms indicating that the response time is limited by the thermal, not mechanical characteristics of the system. In addition, the overshoot in deflection angle is reduced to less than one percent during both rise and fall powers for the 5 ms ramp. Similarly, the settling time of the 5 ms ramp indicates very little ringing. The fall time increased by a factor of two between a 5 ms ramp and a step voltage. It is possible that this may be mitigated by using more sophisticated driving techniques to allow the slope of the voltage ramp to change over time so as to slow the temperature change at the start and increase the rate of change in voltage as the resistance plateaus.

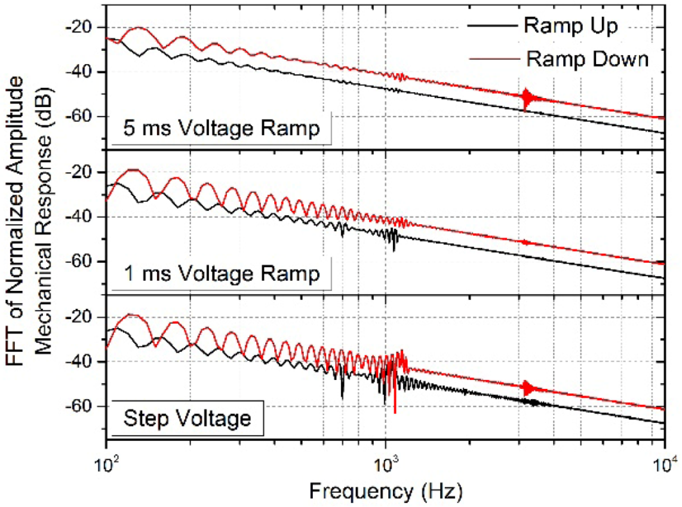

Fig. 10. FFT of the response when heating (Up) and cooling (Down) for varying voltage ramp times. The reduction in response of the first two resonant modes is clear when the voltage ramp is provided over 5 ms when compared to a step voltage.

The ringing for each drive scheme is most obvious when a Fourier transform (FFT) is performed on the mechanical response. Figure 10 illustrates the frequency response of the mirror for each voltage ramp for both rise and fall of the system. The oscillation peaks can be mapped to their respective resonance frequencies from both measured data and simulated resonances. The first mode is a piston mode with a frequency of ~700 Hz and is only apparent during a voltage rise. A more detailed study of the frequency response is required to fully understand the consequence. The second resonance is a torsional mode at approximately 1 kHz. It is clear from the FFT that the torsional mode shifts in frequency between the rise and fall data. Finite element method (FEM) simulations show a frequency shift of approximately 100-200 Hz as the temperature is increased, but a more detailed study is required to fully understand the phenomenon. Similarly, the 3 kHz resonance seen in the FFT data has been observed during frequency sweeps with a lock-in amplifier and PSD system, but the mode shape is not clear at this point in time. FEM simulations show a higher order piston mode at ~2.5 kHz and a torsional mode at ~2.8 kHz. The mechanical response of the mirror wedges was not measured directly. However, it is assumed to be limited thermally as length of the wedges require the mechanical resonance to be ~25 times greater than the bimorph legs, while the time to heat the springs is ~2-3 times longer. Thus, the thermal time constant governs the rate at which the focal length can be changed.

4. Conclusion

A tip-tilt-piston micromirror with wide varifocal range has been demonstrated. The focal length is tunable from –0.48 mm to + 20.5 mm with 27 mW of electrical power. The mirror can be deflected ± 40° along two axes with 90 mW of total electrical power. Vertical displacement of up to 300 μm is possible, however this sets a limit on the minimum focal length of –0.87 mm and any vertical displacement puts a much more stringent limit on the possible deflection angle. Our system also shows a response time of approximately 5 ms for large angles and can be driven such that any ringing is almost completely removed. The

#235441 - $15.00 USD Received 5 Mar 2015; revised 26 Mar 2015; accepted 26 Mar 2015; published 3 Apr 2015

integration of a large range varifocal mirror with steering actuators has implications for both optical systems in research as well as innovative dynamic lighting products. Our design simplifies what would typically be a system of multiple optical components into a single device, therefore reducing both cost and complexity and significantly opening up the possible application space for such mirrors.

Acknowledgments

This work was supported primarily by the Engineering Research Centers Program of the National Science Foundation under NSF Cooperative Agreement No. EEC-0812056.

#235441 - $15.00 USD Received 5 Mar 2015; revised 26 Mar 2015; accepted 26 Mar 2015; published 3 Apr 2015